Material Forming - ESAFORM 2025 Materials Research Forum LLC
Materials Research Proceedings 54 (2025) 1490-1499 https://doi.org/10.21741/9781644903599-161

Expert-informed neural network (EINN) for the forming depth prediction from a small-scale sheet metal forming database

Luca Quagliato[1,a *], Mattia Perin[2,b], Vahid Modanloo[3,c], Taeyong Lee[1,d]

[1]Department of Mechanical and Biomedical Engineering, Ewha Womans University, Seoul, South Korea

[2]Department of Management and Engineering, University of Padua, Vicenza, Italy

[3]Mechanical Engineering Department, Sirjan University of Technology, Sirjan, Iran

[a]lucaq@ewha.ac.kr, [b]mattia.perin@phd.unipd.it,
[c]v.modanloo@sirjantech.ac.ir, [d]tlee@ewha.ac.kr

Keywords: Sheet Metal Forming, Process Modeling, Expert-Informed Neural Network (EINN), Deep Neural Network (DNN), Extreme Gradient Boosting (XGB)

Abstract. It is well established that supervised machine learning (SML) models often perform poorly when presented with new inputs outside their latent space, due to misalignment with the features learned during the training process. Although Physics-Informed Neural Networks (PINNs) have demonstrated promising results, their reliance on physics-based partial differential equations (PDEs) limits their applicability in manufacturing engineering, where PDEs are not easily definable. To overcome this challenge, this work introduces an Expert-Informed Neural Network (EINN), where PDEs are numerically derived based on engineering expertise and incorporated into the backpropagation scheme to enhance extrapolation accuracy. To evaluate the EINN architecture, a dataset comprising 15 finite element analyses (FEA) and 9 cold-warm stamping experiments on 0.1 mm thick pure titanium (Ti) sheets was employed. The EINN was benchmarked against two SML models, Extreme Gradient Boosting (XGB) and Deep Neural Networks (DNN) demonstrating similar training and validation scores with both benchmark models while outperforming them in predicting the forming depth limit in more complex scenarios beyond its original latent space, achieving an average accuracy improvement of over 25%.

Introduction

Process modeling and prediction in manufacturing engineering have attracted the attention of academia and industry for several decades [1]. Although a huge number of contributions dealing with analytical, numerical, and finite element and finite volume analysis are available [2], recent years have seen a spike in artificial intelligence (AI) and machine learning (ML) research [3, 4]. While machine learning (ML) provides a wide array of methodologies [5], recent advancements in manufacturing, process control, and optimization predominantly emphasize ensemble methods [6, 7] and neural networks (NN) [8-10]. On top of that, ML models are also being employed in manufacturing engineering to predict material properties [11] and defects [12]. However, all traditional supervised machine learning (SML) models, regardless of their architecture, share similar issues related to prediction accuracy outside of their latent space. In this regard, the issue is represented by the validity range of the trained model, which is inevitably related to the features and target variables in the training dataset [13].

To address this, an interesting solution is represented by Physics Informed Neural Networks (PINNs) [14] and Gradient-Enhanced Physics-Informed Neural Networks (gPINNs) [15]. The former leverages physics-bounded partial differential equations (PDEs) as a tool to improve the output of the NN to have a better representation of reality, both within and outside of the latent space. The latter employs gradients instead of PDEs at the end of the NN to add an additional tuning layer based on numerical derivatives with respect to features. Both PINNs and gPINNs have been successfully employed in various fields, among them fluid mechanics [16] and inverse structural vibration problems [17]. Considering the improvements demonstrated by PINNs and gPINNs to more traditional SML techniques, this contribution proposes a hybrid modeling between PINNs and gPINNs where gradients are based on engineering knowledge translated into PDEs, to be employed in a PINN-like architecture, thus as an intermediate module between the exit of the NN and the beginning of the backpropagation branch. According to its definition, the developed modeling architecture is defined as an Expert-Informed Neural Network (EINN).

To verify the implemented EINN solution, a sheet metal forming process involving Ti plates was considered. In this regard, a training database (DB) composed of 9 cold-warm stamping experiments and 15 finite element analysis (FEA) simulations on 0.1 mm thick pure Ti sheets was constructed. The size of the training DB was intentionally kept small to benchmark the EINN model performance, with respect to an Extreme Gradient Boosting (XGB) and a Deep Neural Network (DNN) model, in the presence of a limited data scenario, typical of manufacturing engineering. In the DB, process and material parameters were included as features whereas the forming depth magnitude and forming ratio, the latter calculated in terms of the ratio between the achieved depth before tearing and the planned one, were considered target variables. In this regard, the estimation of the forming depth in sheet metal forming is a crucial parameter in the process setting [18, 19] and for this reason, has been considered as the target variable in this contribution.

From the results, no significant differences were observed in terms of training and cross-validation scores among EINN, XGB, and DNN models. On the other hand, when applied on a more complex shape, represented by a metallic bipolar plate (MBP), stamped with the same 0.1 mm Ti sheet material, the EINN solution, boosted by the custom-design PDEs, allowed for a 25% improvement on average in extrapolation performance in comparison to XGB and DNN models.

Materials & Methods

Training Database. The training DB is composed of stamping experiments on 0.1 mm thick commercially pure Ti Gr.1 plates, commonly employed in metallic bipolar plates (MBPs), the latter one considered as validation component and presented in the following section. The material properties were characterized through tensile tests along the parallel (0°), 45°, and transversal (90°) directions to the rolling direction and by employing the ASTM-E8M specimen geometry. Together with the cutting direction, room temperature (RT), 100°C, and 200°C conditions were considered. The resulting true stress-strain curves for the 0° at the three temperatures and the anisotropy coefficients are reported in Fig. 1a. Afterwards, by employing 30 x 20 mm^2 blanks, corrugated plates were manufactured by the tooling equipment of Fig. 1b, as shown in Fig. 1c.

In Fig. 1d, geometrical parameters of the top and bottom dies are S, W, R, and H equal to 1.2, 1.1, 0.2, and 0.75 mm, respectively, with a draft angle θ of 20° and a die clearance of 0.2 mm. The forming depth is considered as the depth of the groove achieved after forming and before tearing as is referred to as h. Accordingly, the forming ratio is defined as h/H (Fig. 1d) and varies from 0, for a flat sheet, and 1, for a fully filled profile where the theoretical depth is 0.75 mm. Although not independent from one another, the consideration of these two target variables allows understanding the influence of pre-processing normalization of the results on the prediction accuracy of the different models. All forming experiments were carried out with a SANTAM press whereas heating to 100°C and 200°C was provided by three cartridges, each one with a Φ17, 800W capacity, and controlled by thermocouples with a ±5°C tolerance. The summary of the experimental levels, together with the lubrication conditions, and measured forming depth and forming ratio are reported in Table 1.

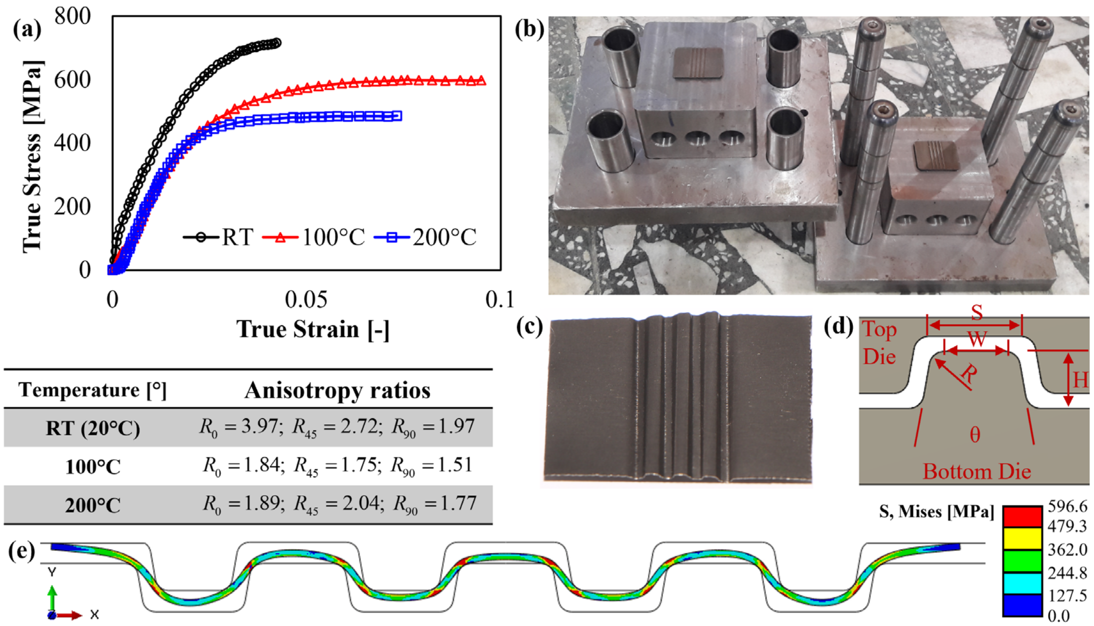

Temperature [°]	Anisotropy ratios
RT (20°C)	$R_0 = 3.97;\ R_{45} = 2.72;\ R_{90} = 1.97$
100°C	$R_0 = 1.84;\ R_{45} = 1.75;\ R_{90} = 1.51$
200°C	$R_0 = 1.89;\ R_{45} = 2.04;\ R_{90} = 1.77$

Figure 1 – (a) True stress-strain curves for the RT, 100°C, and 200°C temperatures and anisotropy ratio for 0°, 45°, and 90° directions. (b) Top and bottom dies for the manufacturing of the (c) corrugated plate and (d) die dimensions. (e) Implemented 2D FEA simulation with von Mises equivalent stress distribution for the last increment before instability is reached.

Table 1 – Experimental settings and results for the forming experiments on the corrugated plate.

Case #	Forming Temperature [°]	Lubricant	Friction coefficient	Stamping speed [mm/min]	Forming depth [mm]	Forming ratio [-]
1	20	Dry	0.30 [20, 21]	0.60	0.40	0.53
2	100			2.40	0.45	0.60
3	200			4.80	0.45	0.60
4	20	Graphite	0.07 [20, 21]	2.40	0.39	0.51
5	100			4.80	0.49	0.65
6	200			0.60	0.44	0.59
7	20	MoS_2	0.10 [20, 21]	4.80	0.48	0.64
8	100			0.60	0.49	0.65
9	200			2.40	0.43	0.57

In addition to the experimental cases, 2-dimensional (2D) finite element analysis (FEA) simulations, developed and validated in a previous work of one of the authors [22], were also considered in the construction of the training DB. A total of 15 FEA cases were implemented in the commercial software (SW) Abaqus/Explicit under cold forming conditions and by expanding the parameters' ranges in comparison to the experimental one. The 2D FEA simulations were implemented with the same die design as Fig. 1b and the dimensions of Fig. 1d, considering both as rigid bodies. The blank sheet was modeled as a 16 mm width and 0.1 mm thickness 2D deformable body and meshed with 640 CPS4R elements (solid reduced-integration elements with hourglass control), of which 3 were along the thickness direction, Fig. 1e. In the FEA simulations, the true stress-strain curve points at the relevant temperature and the settings of Table 3 were considered and a mass scaling factor of 10^{-3} was set to promote convergency while retaining sufficient accuracy. After completing each FEA simulation, step-by-step results were analyzed to identify the point at which instability, and potential tearing, occurred in the metal sheet. This was determined by evaluating the ratio of maximum to minimum equivalent plastic strain (PEEQ). As outlined in prior studies by one of the authors [19], a threshold of 10,000 proved most effective in detecting tearing during the simulations. Accordingly, the forming depth and ratio values presented in Table 2, together with the FEA settings, correspond to the simulation step immediately preceding the PEEQ threshold being reached or exceeded.

Table 2 – Settings and results for the corrugated plates FEA simulations.

Case #	Clearance [mm]	Stamping speed [mm/min]	Friction Coefficient [20,21]	Forming depth [mm]	Forming ratio [-]
10	0.175	2	0.15	0.41	0.55
11	0.15	3.5	0.1	0.43	0.57
12	0.175	2	0.2	0.39	0.52
13	0.175	2	0.1	0.45	0.60
14	0.2	2	0.15	0.44	0.59
15	0.2	0.5	0.2	0.42	0.56
16	0.2	0.5	0.1	0.44	0.59
17	0.2	3.5	0.2	0.43	0.57
18	0.175	0.5	0.15	0.40	0.53
19	0.15	3.5	0.2	0.35	0.47
20	0.15	0.5	0.1	0.43	0.57
21	0.175	3.5	0.15	0.41	0.55
22	0.15	2	0.15	0.40	0.53
23	0.2	3.5	0.1	0.46	0.61
24	0.15	0.5	0.2	0.34	0.45

In summary, each independent row in the training dataset is composed of 17 features, as follows: 10 from the true stress-strain curves from 10% to 100%, for RT, 100°C, and 200°C along 0° directions, 3 anisotropy coefficients, 1 forming temperature, 1 friction factor, 1 stamping speed, and 1 die clearance. These are associated with two target variables, namely the forming depth and forming ratio, measured from the relevant experiment of FEA simulation.

Validation experiments. To validate the EINN model and benchmark it with the XGB and DNN formulations, additional forming experiments were carried out considering the same 0.1 mm thick pure Ti plates, this time with a 210 x 210 mm^2 blank area, but a more complex geometry, as shown in Fig. 2a. The MBP in Fig. 2a is a key component of proton exchange membrane fuel cells (PEMFCs), is composed of an intricate network serpentine (Fig. 2b), and was manufactured under cold forming conditions (room temperature) and with no additional lubrication.

On the formed MBP parts two sections were performed along the A-A and B-B planes, as shown in Fig. 2a and as carried out for the simple corrugated plates in Fig. 1, the forming depth on the locations in sections A-A and B-B were measured by an optical microscope connected to a post-processing SW as detailed in Fig. 2c. The summary of the forming depth and forming ratio measured on the A-A and B-B sections of Fig. 2a are reported in Table 3 and have been employed as the test dataset after the training and validation of the EINN, XGB, and DNN models.

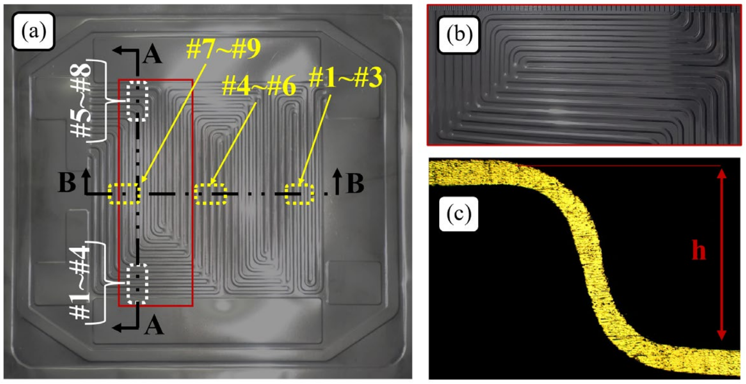

Figure 2 – (a) Manufactured metallic bipolar plate (MBP)with indication of the sections, (b) detailed of the serpentine profile, and (c) optical measuring method for the forming depth.

Table 3 – Forming depth and forming ratio for the MBP Section A and Section B.

MBP (A-A)	Forming depth [mm]	Forming ratio [-]		MBP (B-B)	Forming depth [mm]	Forming ratio [-]
Pos#1	0.298	0.397		Pos#1	0.322	0.429
Pos#2	0.301	0.401		Pos#2	0.325	0.433
Pos#3	0.304	0.405		Pos#3	0.342	0.456
Pos#4	0.353	0.471		Pos#4	0.361	0.481
Pos#5	0.336	0.448		Pos#5	0.358	0.477
Pos#6	0.345	0.460		Pos#6	0.345	0.460
Pos#7	0.313	0.417		Pos#7	0.339	0.452
Pos#8	0.305	0.407		Pos#8	0.336	0.448
Pos#9	0.309	0.412		-	-	-

EINN theoretical background. The EINN model is based on the architecture of a standard DNN algorithm, as in Eq. 1, where the hyperbolic tangent (*tanh*) was employed as activation function, and **x** represents the features' vector. The forward DNN model is defined as in Fig. 3 and has been modified in its backpropagation branch to mimic the behavior of PINNs but defined based on engineering knowledge in terms of numerically derived PDEs, as in gPINNs.

$$\mathbf{h}_i = \tanh\left(\mathbf{W}_i\mathbf{x} + \mathbf{b}_i\right) \quad where \quad \mathbf{x} = \left[x_1, x_2, ..., x_n\right] \in \Re^n \qquad (1)$$

Three features have been selected as critical in the definition of the PDEs, namely *clearance* (*c*), *stamping speed* (*v*), and *friction coefficient* (*μ*) have been connected to three variable features among the remaining 10 relevant for the flow stress and 3 for the anisotropy coefficient. The former are indicated as x_1, x_2, and x_3 whereas the latter as v_1, v_2, and v_3 in Fig. 3. Accordingly, six residuals' formulations are defined as the form of Eq. 2. For a matter of conciseness, only the general formulation for the PDE residuals is reported in Eq. 2, though the specific residuals' equations can be obtained by substituting the relevant feature to the "*x*" in the first- and second-order PDE terms. The last term in Eq. 2, multiplied by the parameter ζ, refers to the standard residuals of the DNN model whereas the *cross-product sum* (CPS) includes the products of first-order derivatives and features to account for inter-features dependency. Accordingly, the residuals at the onset of the backpropagation (Fig. 3) are estimated based on 3 fixed PDEs, in turn based on the critical features discussed above, 3 variable features PDEs, and the standard residual of the DNN, based on the mean square error (MSE) between true and predicted values. The selection of the variable features is based on their effect on the accuracy of the prediction outside of the latent space, as discussed further in the paper. In addition, as shown in Eq. 2, each term in the residuals is multiplied by a constant (α, β, γ, δ, ε, and ζ), for a total of 6 parameters, to be optimized during the tuning of the EINN model. As a final remark, after the residuals' calculation, the solution reverts to a classic NN, though the backpropagation is influenced by the PDEs set in the residuals, thus the gradient of the loss function is used to update weights (**W***ᵢ*) and bias (**b***ᵢ*), as in Eq. 3.

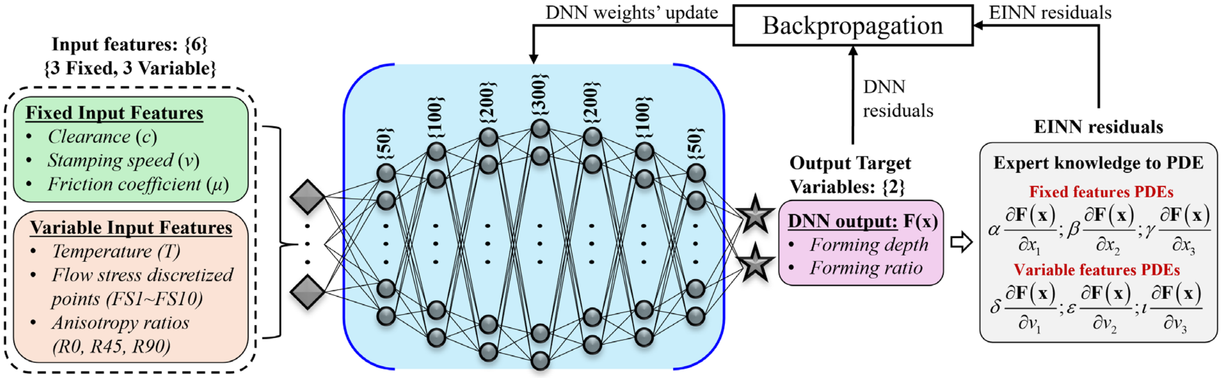

Figure 3 – DNN model architecture and EINN backpropagation module interaction.

$$Res_x = \frac{\partial F}{\partial x} - \left(\alpha \frac{\partial^2 F}{\partial x^2} + \beta x + \gamma \mu + \delta v + \varepsilon CPS + \zeta \frac{\partial F}{\partial y} \right)$$
$$where \quad CPS = \left(\sum_{i \neq j} \frac{\partial F}{\partial x_i} \cdot x_j \right) \quad with \quad x_i, x_j \in \left\{ c, \mu, v, R_0, R_{45}, R_{90} \right\} \tag{2}$$

$$\theta_{t+1} = \theta_t - \eta \nabla_\theta \left(Loss_{tot} \right) \quad where \quad \begin{cases} Loss_{tot} = Loss_F + \sum_{i=1}^{3} Loss_{x,i} + \sum_{i=1}^{3} Loss_{v,i} \\ \theta = \left\{ \mathbf{W}_i, \mathbf{b}_i \right\}_{i=1}^{k} \end{cases} \tag{3}$$

Benchmark models' background. To benchmark the performance of the EINN model, two largely employed SML models were considered. The former is the Extreme Gradient Boosting (XGB) formulation, which is based on a gradient-boosting framework that builds decision trees sequentially, with each tree aiming to correct the errors of the previous one [6]. In the XGB model, the objective function combines the loss function and the regularization term to optimize the model, Eq. 4, where the first term measures the difference between the predicted and true values whereas the second part (regularization term) penalizes model complexity.

$$L(\phi) = \sum_{i=1}^{n} \ell\left(y_i, \hat{y}_i\right) + \sum_{k=1}^{T} \Omega\left(f_k\right) \quad where \quad \Omega\left(f_k\right) = \gamma T + \frac{1}{2} \lambda \left\| \omega \right\|^2 \tag{4}$$

In Eq. 4, y_i are the true values, $\hat{y}_i$ the predictions, T the number of leaves in a tree, γ controls the complexity of the model, λ regularizes the leaf weights, and ω are the leaf weights. The XGB model builds the model iteratively by adding one tree at a time to minimize the objective function, as in Eq. 5, where $f_t\left(x_i\right)$ is the new tree at the *t*-iteration. To determine the structure of the tree at each iteration, the objective function is approximated using a second-order Taylor expansion, as in Eq. 6 where g_i and h_i are the first- and second-order gradients.

$$\hat{y}_i^{(t)} = \hat{y}_i^{(t-1)} + f_t\left(x_i\right) \tag{5}$$

$$L^{(t)} \approx \sum_{i=1}^{n}\left[g_i f_t(x_i) + \frac{1}{2} h_i f_t(x_i)^2 \right] + \Omega\left(f_t\right) \tag{6}$$

As concerns the DNN benchmark model, the structure is the same as Fig. 3 and also represents the starting point for the EINN model. In this regard, the input layer is composed of 6 neurons, equal to the number of input features, followed by $[50, 100, 200, 300]_S$ hidden layers' structure and one output layer with 2 neurons, representative of the two target variables. In both EINN and DNN models, the *tanh* activation function was employed, together with the Adam (Adaptive Moment Estimation) with a learning rate of 10^{-5}, and a loss function based on the Mean Squared Error (MSE). Finally, the batch size was set to 32, and the learning process limit set to a total of 200,000 epochs, with an early stop condition based on a 10^{-3} threshold.

Results and Discussion

The EINN, XGB, and DNN algorithms were implemented in the Phyton/Spyder 3.11 environment considering *pythorch*, *pandas*, *sklearn*, and *numpy* libraries. All codes have been run on a workstation with 13th Gen Intel(R) i5-13500 (2.50 GHz) CPU and 64GB of RAM.

For the EINN model, the first step is represented by the selection of the three variable features to be associated with the fixed features, as per Fig. 3. The selection of specific features is motivated by the will to reduce the complexity of the PDEs in the residuals while including more in-depth optimization through the α, β, γ, δ, ε, and ζ constants of Eq. 2. To this end, a random search to identify the best variable features was carried out based on *temperature*, *flow stress discretized points* from 10% to 100% of the strain, and three *anisotropy ratios* for a total of 73 combinations in a random search scheme, equal to 20% of the total number of possible permutations. This resulted in the identification of anisotropy coefficients (R_0, R_{45}, and R_{90}) to be the variable features having the highest impact on convergence and accuracy. Afterward, the above-mentioned six models' constants were optimized by considering 6 parameters and 3 levels Design of Experiment (DoE) approach based on the Taguchi L18 array, as reported in Fig. 4a. Among the 18 tested configurations, the percentage error slightly varies within the 4.6%~6.2% range for training and 9.8%~11.8% for the validation set, respectively.

For the XGB model, all 17 features (3 fixed and 14 variable) were included in the training associated with a k=5 cross-validation resulting in the optimized hyperparameters being *n_estimators* = 500, *max_depth* = 5, *learning_rate* = 0.005, and *subsample* = 0.6, respectively. The average percentage errors and relevant standard deviations over the 5-folds are equal to 5.9±1.5% and 6.3±1.6% for training and validation, respectively. As concerns the DNN model, the same architecture of the EINN formulation was employed except for the customized backpropagation module (Fig. 3). After an initial calibration where random triplets of features were tested, the best combination of variable features is represented by the three anisotropy coefficients (R_0, R_{45}, and R_{90}), together with the fixed features (*clearance*, *friction coefficient*, and *stamping speed*). With this configuration, the percentage errors for training and validation are equal to 5.8% and 9.9% respectively, and the DNN model converged after approximately 7,000 epochs. Besides, the XGB model was trained in approximately 25 minutes, whereas the constants optimization for the EINN formulation required ~5,000 minutes. After the optimized constants for the PDEs system at hand are optimized, both EINN and DNN models can be trained in approximately 40 minutes.

As summarized so far, the XGB model shows good performance both in training and validation, also thanks to the *k=5* cross-validation. As per the EINN model, the lowest percentage error of 4.6% for the training is associated with a higher validation error of 9.8%, whereas the DNN model stands approximately in between these two formulations. Although some differences arise, EINN, XGB, and DNN have similar training and comparable performance on validation, but it should also be noted that both training and validation are based on the experimental and FEA databases of the corrugated plate and not the MBP data points outside of the latent space.

(a) EINN PDEs setting levels

Run	α	β	γ	δ	ε	ζ
1	1	1	1	1	1	1
2	1	1	0.5	0.5	0.5	0.5
3	1	1	0.1	0.1	0.1	0.1
4	1	0.5	1	1	0.5	0.1
5	1	0.5	0.5	0.5	0.1	1
6	1	0.5	0.1	0.1	1	0.5
7	1	0.1	1	0.5	1	0.1
8	1	0.1	0.5	0.1	0.5	1
9	1	0.1	0.1	1	0.1	0.5
10	0.5	1	1	0.1	0.1	0.5
11	0.5	1	0.5	1	1	0.1
12	0.5	1	0.1	0.5	0.5	1
13	0.5	0.5	1	0.5	0.1	1
14	0.5	0.5	0.5	0.1	1	0.5
15	0.5	0.5	0.1	1	0.5	0.1
16	0.5	0.1	1	0.1	0.5	1
17	0.5	0.1	0.5	1	0.1	0.5
18	0.5	0.1	0.1	0.5	1	0.1

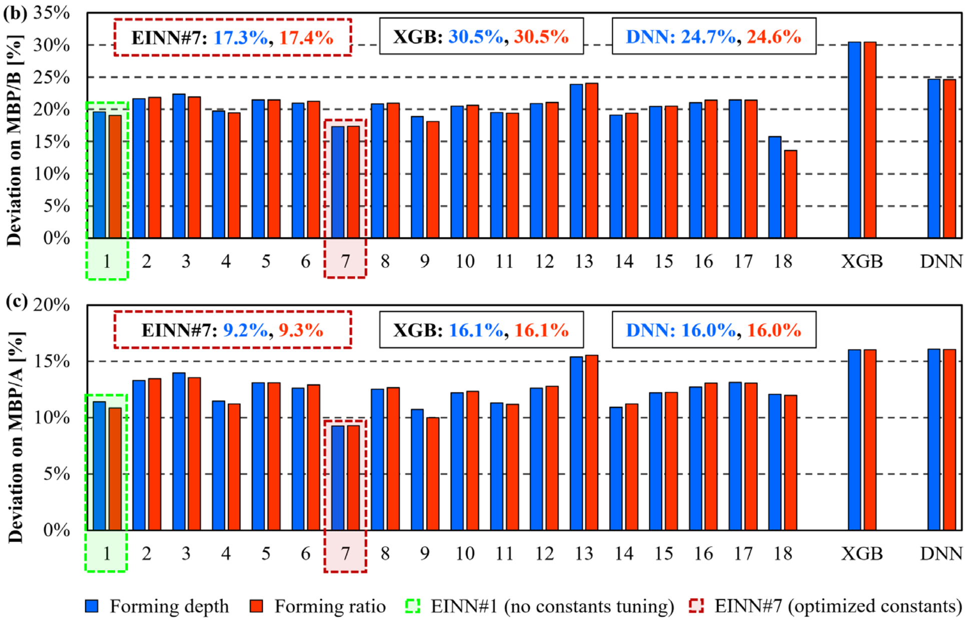

Figure 4 – (a) Taguchi L18 array with settings for the constants in the residuals for the EINN model. Percentage error for the 18 configurations of the EINN model, according to (a), and for the benchmark XGB and DNN for (b) section A-A (MBP/A) and (c) section B-B (MBP/B).

In this regard, the performances of the EINN, XGB, and DNN models outside of the latent space have been assessed by applying them to the 9 points and 8 points of section A-A and B-B for the MBP component, Fig. 2. The results, summarized in Fig. 4b and 4c, show the percentage error in predicting the forming depth (blue) and forming ratio (red) and, for the case of the EINN model, show all 18 configurations of Fig. 4a where different constants settings were considered. It should be noted that section A-A is oriented transversely to the profile of the corrugated plate employed for the training thus, due to the difference in the flow stress, it further away from the training latent space than section B-B.

Considering Fig. 4b and 4c, although EINN, DNN, and XGB model showed similar performance within the latent space, when it comes to unseen data having different features' distribution, both XGB and DNN models' performance dropped significantly. For section A-A, Fig. 4b, the EINN model has generally better performance than both benchmarks, except for EINN#13 which is close to the DNN result. Overall, EINN#7 shows a percentage error reduction of 43.1% to the XGB model and 30.4% to the DNN model. Moreover, although EINN#7 is the second-best model among the 18 tested for section A-A, it is also the one with the most consistent performance improvement across both A-A and B-B sections. In this regard, also for the case of section B-B, the percentage error reduction granted by the EINN#7 model is equal to 42.2% for the XGB and 42.2% for the DNN model, respectively. At this point, it is worth mentioning that, when applied to data points with low similarity with the latent space, section A-A of Fig. 4b, the DNN model performs better than the XGB algorithm and can catch more complex features' interactions. However, when applied to section B-B (Fig. 4c), the similarity of the material properties with those of the corrugated plate makes the XGB and DNN have similar performance. In addition, if no results on the target component outside of the training latent space are known, the EINN model can still be applied with all its 6 PDEs constants with the same weight equal to one. This is the case of EINN#1, Fig. 4, which shows slightly lower improvements in comparison to EINN#7, equal to 36.5% and 22.3% for section A-A and 30.5% and 31.7% for section B-B, and for the XGB and DNN models respectively. Generally speaking, the average deviations of all 18 EINN models of Fig. 4 are equal to 16.3%, in contrast to 23.7% for the XGB and 20.3% for the DNN model, with relevant improvements of 31.2% and 19.7%, respectively, and show the improvement granted by employing the EINN formulation over more generic models.

Conclusions & Outlook

This research focused on the development of a customizable PINN formulation where the PDEs in the backpropagation are based on engineered PDEs rather than physic-bounded laws and defined as the EINN model. Experimental and FEA results for the stamping of simple corrugated plates made of pure Ti sheets were employed for the initial training and validation, resulting in similar deviations to the XGB and DNN models, employed as benchmarks. However, when the trained models were applied to more complex geometries, not included in the training, the optimized EINN solution allowed for average reductions in the forming depth and ratio deviation of ~43% and ~36%, to XGB and DNN models, respectively. The results of this contribution cast light onto the necessity of developing *ad-hoc* solutions for SML modeling in manufacturing engineering, and that the customization of the backpropagation branch by user-defined PDEs is a viable option. For these reasons, the proposed class of solutions might be of interest to industrial engineers interested in developing prediction models with a higher degree of generalization and longevity.

References

[1] J.P.T. Mo, S.C.P. Cheung, R. Das, Demystifying Numerical Models: Step-by-Step Modeling of Engineering Systems, first ed., Butterworth-Heinemann, 2019. https://doi.org/10.1016/C2015-0-05428-4

[2] M. Schwenzer, M. Ay, T. Bergs, D. Abel, Review on model predictive control: an engineering perspective, Int. J. Adv. Manuf. Technol. 117 (2021) 1327–49. https://doi.org/10.1007/s00170-021-07682-3

[3] O. Mypati, A. Mukherjee, D. Mishra, S.K. Pal, P.P. Chakrabarti, A. Pal, A critical review on applications of artificial intelligence in manufacturing, Artif. Intell. Rev. 56 (2023) 661–768. https://doi.org/10.1007/s10462-023-10535-y

[4] J. Cao, M. Bambach, M. Merklein, M. Mozaffar, T. Xue, Artificial intelligence in metal forming, CIRP Ann. (2024) 1–27. https://doi.org/10.1016/j.cirp.2024.04.102

[5] I. Mirandola, G.A. Berti, R. Caracciolo, S. Lee, N. Kim, L. Quagliato, Machine learning-based models for the estimation of the energy consumption in metal forming processes, Metals 11 (2021). https://doi.org/10.3390/met11050833

[6] S. Lee, J. Park, N. Kim, T. Lee, L. Quagliato, Extreme gradient boosting-inspired process optimization algorithm for manufacturing engineering applications, Mater. Des. 226 (2023) 111625. https://doi.org/10.1016/j.matdes.2023.111625

[7] S.M. Najm, I. Paniti, Investigation and machine learning-based prediction of parametric effects of single point incremental forming on pillow effect and wall profile of AlMn1Mg1 aluminum alloy sheets, J. Intell. Manuf. 34 (2023) 331–67. https://doi.org/10.1007/s10845-022-02026-8

[8] F. Mumali, Artificial neural network-based decision support systems in manufacturing processes: A systematic literature review, Comput. Ind. Eng. 165 (2022) 107964. https://doi.org/10.1016/j.cie.2022.107964

[9] S. Duan, D. Kozjek, E. Mehr, M. Anders, J. Cao, Forming force prediction in double-sided incremental forming via GNN-based transfer learning, J. Manuf. Process. 120 (2024) 867–77. https://doi.org/10.1016/j.jmapro.2024.04.093

[10] H.R. Attar, H. Zhou, A. Foster, N. Li, Rapid feasibility assessment of components to be formed through hot stamping: A deep learning approach, J. Manuf. Process. 68 (2021) 1650–71. https://doi.org/10.1016/j.jmapro.2021.06.011

[11] S.K. Dewangan, R. Jain, S. Bhattacharjee, S. Jain, M. Paswan, S. Samal, et al., Enhancing flow stress predictions in CoCrFeNiV high entropy alloy with conventional and machine learning techniques, J. Mater. Res. Technol. 30 (2024) 2377–87. https://doi.org/10.1016/j.jmrt.2024.03.164

[12] S. Feng, H. Zhou, H. Dong, Using deep neural network with small dataset to predict material defects, Mater. Des. 162 (2019) 300–10. https://doi.org/10.1016/j.matdes.2018.11.060

[13] Y. Wang, R.D. King, Extrapolation is Not the Same as Interpolation, Lecture Notes in Comp. Sci. 14276 (2023) 277–93. https://doi.org/10.1007/978-3-031-45275-8_19

[14] M. Raissi, P. Perdikaris, G.E. Karniadakis, Physics Informed Deep Learning (Part II): Data-driven Discovery of Nonlinear Partial Differential Equations, (2017) 1–22. https://doi.org/10.48550/arXiv.1711.10566

[15] J. Yu, L. Lu, X. Meng, G.E. Karniadakis, Gradient-enhanced physics-informed neural networks for forward and inverse PDE problems, Comput. Methods Appl. Mech. Eng. 393 (2022). https://doi.org/10.1016/j.cma.2022.114823

[16] S. Cai, Z. Mao, Z. Wang, M. Yin, G.E. Karniadakis, Physics-informed neural networks (PINNs) for fluid mechanics: a review, Acta Mech. Sin. 37 (2022) 1727–38. https://doi.org/10.1007/s10409-021-01148-1

[17] T. Chatterjee, M.I. Friswell, S. Adhikari, H.H. Khodaparast, Gradient Enhanced Physics-informed Neural Networks for Digital Twins of Structural Vibrations, Proc. of the 32nd Europ. Safety and Rel. Conf. (2023) 2586–93.

[18] V. Modanloo, H. Talebi-Ghadikolaee, V. Alimirzaloo, M. Elyasi, Fracture prediction in the stamping of titanium bipolar plate for PEM fuel cells, Int. J. Hyd. En. 46 (2021) 5729–39. https://doi.org/10.1016/j.ijhydene.2020.11.088

[19] S. Lee, Y. Lim, L. Galdos, T. Lee, L. Quagliato, Gaussian process regression-driven deep drawing blank design method, Int. J. Mech. Sci. 265 (2024) 108898. https://doi.org/10.1016/j.ijmecsci.2023.108898

[20] J. Ma, H. Yang, H. Li, D. Wang, G.J. Li, Tribological behaviors between commercial pure titanium sheet and tools in warm forming, Trans. Nonferrous Met. Soc. China 25 (2015) 2924–31. https://doi.org/10.1016/S1003-6326(15)63918-8

[21] W. Więckowski, J. Adamus, M. Dyner, M. Motyka, Tribological aspects of sheet titanium forming, Materials 16 (2023). https://doi.org/10.3390/ma16062224

[22] Modanloo V, Alimirzaloo V, Elyasi M, Optimal Design of Stamping Process for Fabrication of Titanium Bipolar Plates Using the Integration of Finite Element and Response Surface Methods, Arab J. Sc. Eng. 45 (2020) 1097–1107. https://doi.org/10.1007/s13369-019-04232-8